Desalination and Water Treatment
www.deswater.com

doi: 10.5004/dwt.2020.26138

200 (2020) 252–261
October

Oxidation–adsorption of arsenite contaminated water over ceria nanorods

Suttikorn Suwannatrai[a], Dickson Y.S. Yan[b], Jakkapop Phanthasri[a], Pummarin Khamdahsag[c], Suttipong Wannapaiboon[d], Visanu Tanboonchuy[a,e,*]

[a]*Department of Environmental Engineering, Faculty of Engineering, Khon Kaen University, Khon Kaen, 40002 Thailand, Tel. +664-336-2140; emails: visanu@kku.ac.th (V. Tanboonchuy), suttigon7@hotmail.com (S. Suwannatrai), jakkapop@kkumail.com (J. Phanthasri)*
[b]*Faculty of Science and Technology, The Technological and Higher Education Institute of Hong Kong, New Territories, Hong Kong, email: dicksonyan@vtc.edu.hk (D.S. Yan)*
[c]*Environmental Research Institute, Chulalongkorn University, Bangkok 10330, Thailand, email: pummarin.k@chula.ac.th (P. Khamdahsag)*
[d]*Synchrotron Light Research Institute (Public Organization), Nakhon Ratchasima 30000, Thailand, email: suttipong@slri.or.th (S. Wannapaiboon)*
[e]*Research Center for Environmental and Hazardous Substance Management (EHSM), Khon Kaen University, Khon Kaen 40002, Thailand*

Received 31 October 2019; Accepted 14 May 2020

ABSTRACT

The dominant arsenic oxidation state in groundwater as As(III) is more difficult to remove than As(V). To achieve higher As(III) removal, ceria (CeO_2) nanorods characterized by Brunauer–Emmett–Teller, X-ray diffraction, scanning electron microscopy, Fourier transform infrared, and X-ray absorption spectroscopy were successfully used to combine oxidation and adsorption processes. Results showed that when calcination temperature increased surface area decreased, whereas crystallite size increased. Batch experiments indicated that the arsenic removal process was accurately described by a pseudo-second-order kinetic model with maximum removal capacities of 21.27 mg/g. X-ray absorption near-edge structure (XANES) of the solid-phase confirmed that CeO_2 adsorbed As(III) with partial As(III) oxidization to As(V) on the surface. Further evidence of the mechanisms for As(III) removal was demonstrated by the hydroxyl group in the sorption and As(III) forming inner-sphere monodentate and bidentate complexes on the interface of the CeO_2 solid phase. As(III) oxidization to As(V) during the sorption process suggested that CeO_2 had high potential to remove As(III) from contaminated water.

Keywords: Adsorption; Arsenic complexes; Arsenite; Ceria; Cerium oxide; Oxidation

1. Introduction

Arsenic (As) contamination in groundwater is an issue of high concern because As is both toxic and carcinogenic. Long-term consumption of high arsenic-contaminated water may lead to cancer of the skin, lungs, liver, and black foot disease [1–4]. Countries affected by high arsenic contamination include Bangladesh, Cambodia, China, India, Nepal, Taiwan, and Thailand [5,6]. Considering the health risks, the World Health Organization has set maximum concentration for arsenic in drinking water at 10 μg/L [7]. Arsenite (As(III)) and arsenate (As(V)) are the two major arsenic species in aqueous systems depending on redox and pH conditions [8]. As(III) exists in anaerobic underground water mainly as $HA_sO_3^{2-}$,

* Corresponding author.

$H_2AsO_3^-$, and H_3AsO_3, while As(V) in the surface water is predominantly presented as H_2AsO^{4-}, $HAsO_3^{2-}$, and H_3AsO_4) [9,10]. Ratios of As(III)/As(total) at depth of 30–40 m have been reported in aquifers in the range of 0.6–0.9 [11,12]. This is a matter of great concern since As(III) is 60 times more toxic than As(V) [13].

As(III) exists in an uncharged form as H_3AsO_3 at the typical pH of water and removal of As(III) is more difficult than As(V). To achieve greater As(III) removal efficiency, treatment processes require pre-oxidation of As(III) to As(V). This leads to increased operational costs and also produces some secondary pollution problems.

Many technologies including injection of oxygen or ozone [14], the Fenton process [15,16], biological oxidation [17,18], photocatalytic oxidation [19,20], and electro-oxidation [21], have been widely studied for the oxidation of As(III). However, each faces one or more limitations such as the addition of oxidants or catalysts, extra energy input, and separation of the added catalyst, while some oxidants may lead to the formation of toxic disinfection byproducts. Furthermore, the oxidized As(V) may be reduced to As(III) and become more mobile under certain conditions [12]. Therefore, new economical and cost-effective materials are required that can combine the oxidation and adsorption remediation processes as an efficient and effective method to remove As(III) without the need for pretreatment. Previous studies have shown that Fe(oxyhydr)oxides [22], Fe-sulfide [23], nano-iron/oyster shell composites [24], and zero-valent iron [25] are effective for As(III) removal.

Ceria (CeO_2), showed efficient arsenic removal over a pH range from 3 to 11 [26], particularly toward As(III) with a high content of hydroxyl groups suggested as responsible for its excellent performance. Moreover, despite the rare earth terminology, ceria and other cerium salts are cheap and show potential as cost-competitive materials. Ceria has a fluorite structure and is an important material with good mechanical, chemical, and thermal stability [27]. Ceria synthesized through a combined oxidation and adsorption process was successfully used to remove As(III) [28], however, high calcination temperature was required which increased synthesis cost and impacted CeO_2 crystal characteristics such as pore size and surface hydroxy groups. Ceria synthesis at low calcination temperature for the uptake of As(III), adsorption performance during high concentration As(III) uptake, and the mechanism of adsorption have yet to be studied and reported using advanced analytical tools.

Here, CeO_2 was prepared by a simple precipitation process with calcination in a furnace at different temperatures. The kinetic and isotherm of adsorbent with high sorption capacity for As(III) was prepared and used to remove As(III) from synthetic water. Sorption behaviors, especially sorption capacity, were investigated, and CeO_2 was characterized by X-ray diffraction (XRD), Brunauer–Emmett–Teller (BET) technique, and point of zero charge (pH_{pzc}). The mode of As(III) sorption onto CeO_2 before and after processing is poorly documented. Our main goal was to better understand the cause of any changes in apparent surface reactivity by determining the nature of As surface complexes using X-ray absorption near-edge structure (XANES). Proposed mechanisms on the surface of CeO_2 were discussed.

2. Materials and methods

2.1. Materials

Chemical reagents used for CeO_2 synthesis included $Ce(NO_3)_3{\cdot}6H_2O$ (99%) (Merck) and NaOH (Merck). The As(III) stock solution was prepared by dissolving $NaAsO_2$ (Merck). NaCl was also used in the ionic strength experiment. All chemical solutions were prepared with deionized water (18.2 MΩ Mill-Q).

2.2. Preparation of CeO_2

Ceria was synthesized by the hydrothermal method under autogenous pressure and used as the Ce^{3+} ion and OH^- ion precursors in all reactions performed toward the synthesis of pure CeO_2. In this study, 1:4 mol of Ce^{3+} and OH^- was rapidly dissolved in 100 mL deionized water. When the NaOH solution was added, the reaction started, and a white Ce(OH) precipitate was formed. The solution was kept in an ambient environment with stirring for 30 min before heating at 110°C for 6 h in a Teflon-lined stainless-steel autoclave. After cooling to room temperature, the precipitate was collected by centrifugation (5 min at 5,000 rpm) and washed with DI water several times to remove excess ionic remnants. Finally, aliquots of the precipitate were calcined in a furnace at different temperatures (105°C–550°C) overnight.

2.3. Characterization of CeO_2

The crystal structure of CeO_2 was characterized by an X-ray powder diffractometer (XRD) (D8 Discover, Bruker AXS) using Bragg-Brentano geometry, equipped with a theta–theta goniometer system with a rotating sample holder. The XRD patterns were collected using Cu Kα radiation (λ = 0.1514 nm) at 40 kV and 40 mA with a scan range of 20°–80°. BET specific surface area was measured by nitrogen adsorption–desorption isotherms (TriStar ll 3020, Micromeritics) to analyze the specific surface area of the CeO_2. A scanning electron microscopy (SEM) (Hitachi, S-3000N) was used to analyze the surface structure and morphology of CeO_2. Prepared samples were analyzed by SEM at an acceleration of 15 kV. Functional group analysis was performed by a Fourier transform infrared spectrometer (FTIR) at a wave-number range of 400–4,000 cm^{-1} (Tensor 27, Bruker). Surface chemical states of As on the CeO_2 surface and nature of Ce surface complexes were determined using As and Ce K-edge XANES with analysis at Beamline BL1.1 at the Synchrotron Light Research Institute (SLRI), Thailand. Reference compounds included Au^0 and V^0 foil, As(III) 5.0 mM, and As(V) 5.0 mM. All spectra were recorded in fluorescence and transmission mode using a 19-element Ge detector due to the low concentration of As.

2.4. Batch experiments

Experiments were conducted to examine the kinetics and isotherms. Experiments to determine the kinetics of the As(III) removal reaction with CeO_2 at room temperature were carried out by batch method. Here, 500 mL of As(III) solution of C_0 from 50 mg/L was mixed with 0.5 g of CeO_2 into a 600 mL beaker and agitated at 200 rpm using a speed

adjustable agitator, with monitoring of pH and oxidation-reduction potential (ORP). The CeO_2 particles were separated by a syringe filter 0.45 μm and analyzed for residual arsenic concentration. To investigate isotherms, 50 mL of As(III) solution of C_0 (mg/L) ranging from 1.0 to 80.0 was mixed with 0.05 g of CeO_2 in a centrifugal tube, and then subjected to 50 rpm for 30 min before separating the CeO_2 particles using a syringe filter 0.45 μm.

After processing, the material was filtrated from solution using a 0.45 μm syringe filter, and As(V) was separated from the solution using an anionic resin-exchange cartridge (A502P, Purolite) as in our previous study [29]. As(V) was retained in the cartridge while As(III) was allowed to pass through. The As(III) concentration was then analyzed by an inductively coupled plasma optical emission spectrometer (ICP-OES, PerkinElmer Optima 8000). As(V) concentration was obtained by subtracting the measured As(III) concentration from total arsenic concentration.

3. Results and discussion

3.1. Characterization of CeO_2

The XRD analysis identified a single crystalline phase in the calcination products at the temperature range of 105°C–550°C with CeO_2 presenting as a cubic fluorite-type structure. With increasing calcination temperature, the diffraction peaks narrowed as the crystallites grew and acquired a more ordered structure [30]. Fig. 1 shows X-ray diffractogram patterns of synthesized CeO_2. Five samples showed typical CeO_2 XRD patterns at around 2θ = 28.5°, 33.0°, 47.4°, 56.3°, 59.3°, 69.6°, 76.7°, and 79.1° corresponding to the (111), (200), (220), (311), (222), (400), (331), and (240) crystalline planes, respectively of the pure cubic phase. All diffraction peaks indicated a ceria fluorite structure (JCPDS 00–034–0394). Pure phase CeO_2 was formed at a high calcination temperature of 550°C, confirming the synthesis as similar to pure CeO_2.

The broadening of XRD peaks provided a convenient method for measuring particle sizes. As crystallite size decreased, the width of the diffraction peaks increased. The average crystallite size was estimated using the Debye-Scherrer equation:

$$D = \frac{C\lambda}{\beta\cos\theta} \tag{1}$$

where D is the crystallite size, C is a numerical constant (0.9), λ is the wavelength of X-rays (CuKα radiation, λ = 1.514 Å), β is the effective peak broadening taken as the full width at half maximum (FWHM) (in radians), and θ is the diffraction angle for the peak. The Crystallite size of the particles was determined using the Debye-Scherrer formula. The XRD data revealed average sizes of CeO_2 as 9.96, 10.20, 10.71, 13.38, and 14.28 nm for products prepared at 105°C, 250°C, 350°C, 450°C, and 550°C, respectively (Fig. 1). A previous report determined average crystallite size of CeO_2 prepared by thermal decomposition of cerous nitrate as 6.45 nm [31], while the increase of hydrothermal temperature led to the formation of nanocubes with narrower XRD diffraction peaks, indicating an incremental increase of mean crystallite size by up to 30–40 nm at 180°C [32]. Moreover, particle size increase with elevating reaction temperature inferred that particle growth rate was predominant over the nucleation rate [33].

Specific surface area is an important parameter in the adsorption process. Fig. 2 shows that the BET surface area

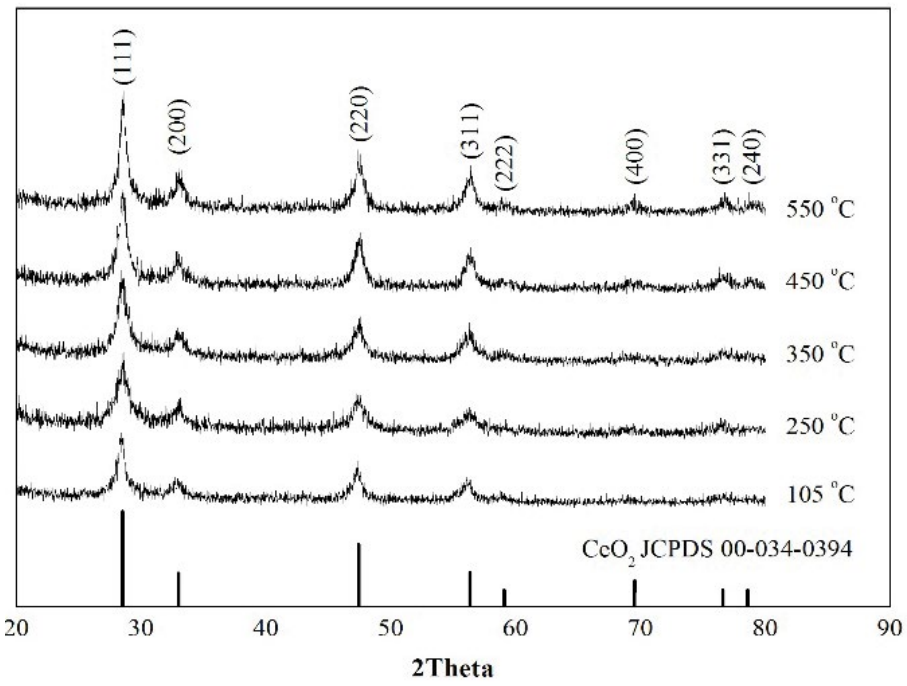

Fig. 1. XRD patterns of CeO_2 synthesized at different calcination temperatures of 105°C to 550°C.

of CeO_2 decreased as calcination temperature increased [34]. Surface area reduced from 74.2 to 41.1 m^2/g with the increase in calcination temperature from 105°C to 550°C, signaling an acceleration of crystallite growth in CeO_2–550°C. Images of SEM surface morphology micrographs for three different calcination temperatures are shown in Fig. 3a. At a temperature of 150°C, ceria nanorods are mainly formed with a very rough and uneven surface containing numerous pits and pores [32]. However, the surface of CeO_2 dried at 105°C shows highly crystalline nanorods evenly distributed over the surface. When the temperature increased, the appearance of crystalline rods on the surface of CeO_2 decreased as presented in Figs. 3b–d. This occurred because of rising calcination temperature in the range 300°C–550°C caused increased particle size growth. Moreover, CeO_2 calcined above 1,070°C had the same density (=99.8%) and particle size increased rapidly to 48 nm [35].

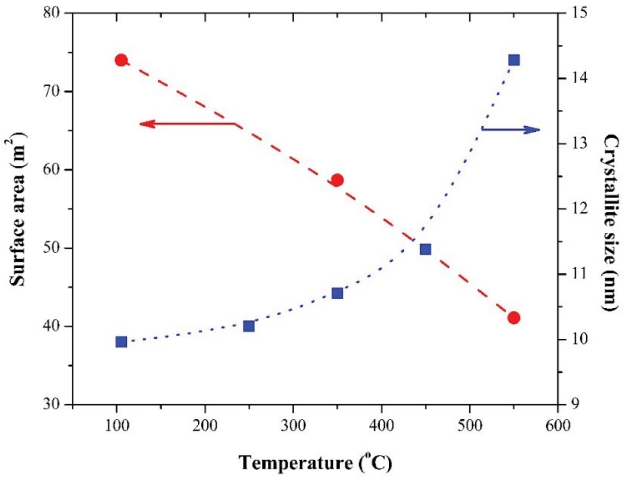

Fig. 2. Characteristics of CeO_2 from XRD patterns and BET analysis.

Relative reductions of surface area and morphology for CeO_2 material at higher calcination temperatures resulting from the rapid growth of crystals were attributed to shrinkage and agglomeration to larger clusters of metallic oxide particles [34]. Decrease of surface area and larger pores resulted in sintering, leading to reduced activity of the adsorbent due to pore elimination and formation of dense solid. Hence, a large surface area is important for high adsorption performance.

The point of zero charge (pH_{pzc}) of CeO_2 can be evaluated by determining the pH value at which the zeta potential is zero. The pH_{pzc} is used to qualitatively assess the polarity of the adsorbent surface charge [36]. At $pH < pH_{pzc}$, the adsorbent has a positive surface charge and can act as an anion exchanger, while at $pH > pH_{pzc}$ the surface charge of the adsorbent is negative and beneficial for adsorbing cations. The pH_{pzc} of CeO_2 is presented in Fig. 4 at about 5.8. The pH value during the adsorption experiment was 6.0–6.50; therefore, a negative charge of the CeO_2 surface was presented. However, under different pH conditions, arsenic species may change to various forms. As(III) exists

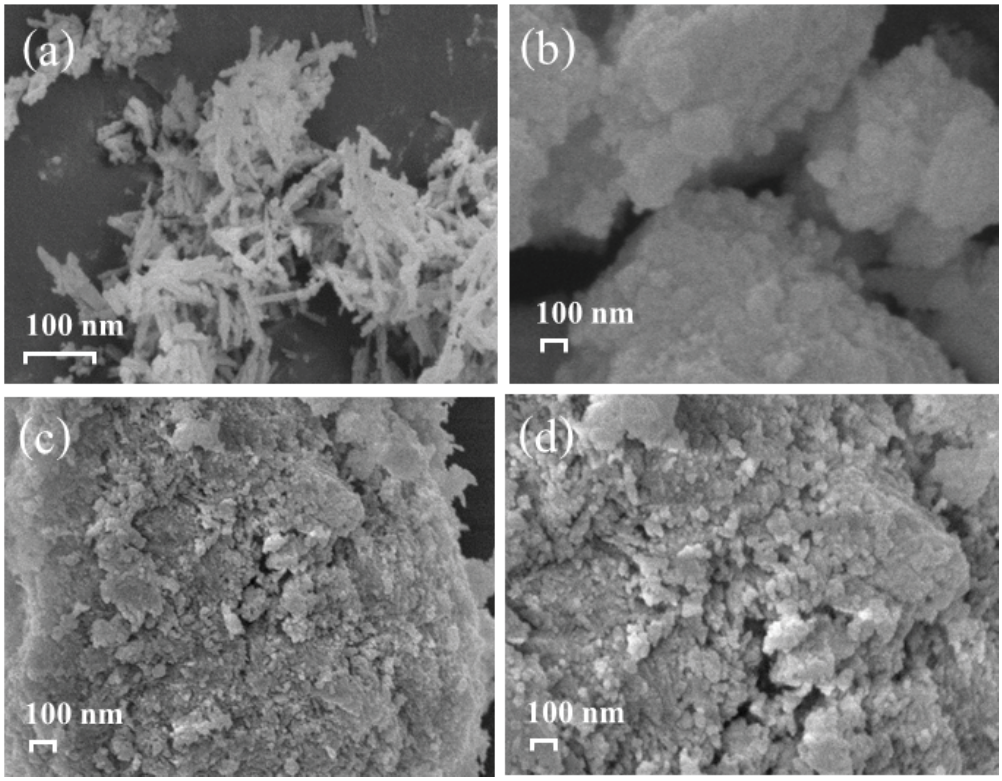

Fig. 3. SEM images of CeO_2 at difference calcination temperatures (a) 105°C, (b) 250°C, (c) 350°C, and (d) 550°C.

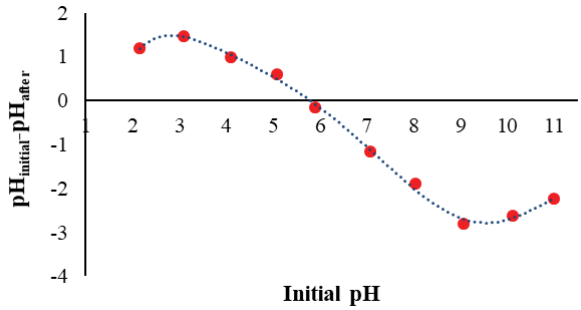

Fig. 4. Zeta potential of CeO_2 samples under various pH values.

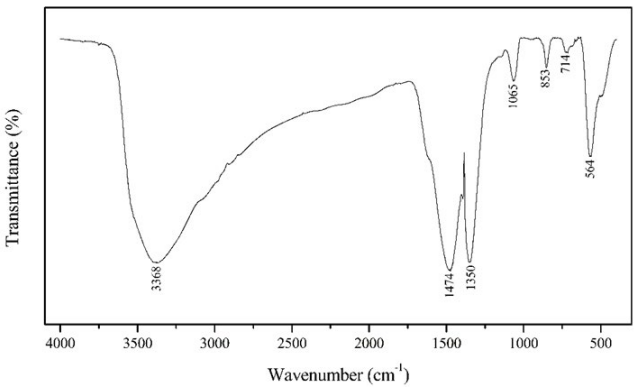

Fig. 5. FTIR spectra of CeO_2 at 250°C calcination temperature.

mainly as H_3AsO_3, a neutral species, when pH is less than 9.2 (pKa_1 = 9.2) [26]. Thus, in this experiment, the pH range of the solution used in this study is probably not playing a role in arsenite removal.

The FTIR spectra of CeO_2 prepared by the simple precipitation process with synthesis at low calcination temperature are shown in Fig. 5. Bands at 545 and 750 cm^{-1} are due to Ce–O stretching vibration, while bands at 1,379 and 1,539 cm^{-1} result from C–O stretching vibration. The band at 1,065 cm^{-1} is due to -NH stretching vibration, and the band at 3,412 cm^{-1} is caused by O–H bond vibrations of water absorbed from moisture. These variable peaks revealed that functional groups such as –OH and C–OH were involved in the adsorption reaction of As(III) ions on CeO_2 [37,38]. Similar results were also deduced for possible adsorption mechanisms for As(III) removal by CeO_2 and these are discussed later.

3.2. Arsenite removal capacity testing

3.2.1. Effect of calcination temperature on As(III) removal

The effect of initial calcination temperature on the rate of As(III) removal is shown in Fig. 6 as a plot of dimensionless concentration vs. time for calcination temperature ranging from 105°C to 550°C. Removal capacity between different calcined products varied from 8.75, 8.94, 7.88, 8.38, and 7.59 mg/g for 105°C, 250°C, 350°C, 450°C, and 550°C, respectively. The CeO_2 material calcined at 250°C showed maximum removal capacity, confirming that the release of residual chemisorbed water and organic residues as NO_3 [39] inhibited arsenic removal. Reaction by-products occurring during the CeO_2 synthesis process are shown as Eqs. (2)–(6).

$$4NaOH_{(s)} \rightarrow 4Na^{+}_{(aq)} + 4OH^{-}_{(aq)} \quad (2)$$

$$Ce(NO_3)_3{\cdot}6H_2O_{(s)} \rightarrow Ce^{3+}_{(aq)} + 3NO^{-}_{3(aq)} + 6H_2O_{(aq)} \quad (3)$$

$$Ce^{3+}_{(aq)} + 4OH^{-}_{(aq)} + xH_2O_{(aq)} \rightarrow Ce(OH)_4{\cdot}xH_2O_{(s)} \quad (4)$$

$$Ce(OH)_4{\cdot}xH_2O_{(s)} \rightarrow Ce(OH)_{4(s)} + xH_2O_{(g)} \quad (5)$$

$$Ce(OH)_{4(g)} \rightarrow CeO_{2(s)} + 2H_2O_{(g)} \quad (6)$$

These reactions are consistent with the crystal size and surface area of CeO_2. The removal capacity of CeO_2 depends on various factors such as surface area, porosity, and surface morphology. However, the chemical characteristics of CeO_2 change on heating. The O/Ce ratio decreased with increasing calcination temperature, while the abundance of O–Ce^{3+} and hydroxyl groups also decreased at higher calcination temperatures [30].

The calcination temperature of CeO_2 at 250°C gave the highest removal capacity. As(III) uptake capacities were determined as a function of time to deduce an optimal contact time for adsorption of As(III) on CeO_2. The amount of As(III) on each CeO_2 sample was calculated by the difference between As(III) content in influent solution and effluent solution expressed as a percentage (C/C_0).

Variation of C/C_0 as a function of time is shown in Fig. 6. The significantly higher arsenic removal efficiency was obtained in the first 10 min. The concentration of As(III) in aqueous solution reduced from 42.29 to 14.68 mg/L in 10 min, revealing that As(III) was quickly removed by CeO_2, and then decreased steadily with increasing reaction time. The optimal time required for CeO_2 to achieve maximum removal efficiency (77%) was 30 min. However, As(III) began to change to As(V) at about 60 min, and this continuously increased to 120 min, indicating that CeO_2 oxidized As(III) to As(V). Additionally, As(III) in aqueous solution was partially oxidized because As(V) was detected in the As(III)-CeO_2 system as shown in Fig. 7.

Ceria is often considered an active catalytic support material due to its excellent reducibility, oxygen transport properties [40], and as a catalyst for oxidation processes [41], resulting in a transfer of electrons to As(III) on the surface of CeO_2. When As(III) receives oxygen electrons it oxidizes to As(V) according to the CeO_2 redox equation. The analysis demonstrated that As(III) in aqueous solution was partially oxidized to As(V), while As(V) did not reduce to As(III). Similar results were also deduced from arsenic speciation on the solid-phase interface by XANES, and these are discussed as follows.

3.2.2. Kinetic model and isotherm analysis of As(III) removal

A pseudo-second-order kinetic model was fitted to the experimental data of arsenic removal by CeO_2 to better understand the reaction kinetics. The expression of this model is presented as Eq. (7):

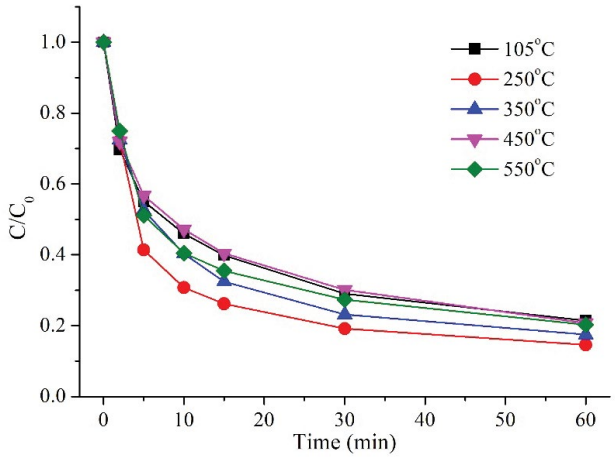

Fig. 6. Adsorption of As(III) onto various calcined CeO_2 samples as a function of calcination temperature (°C) (experiment conditions: CeO_2 = 0.1 g and As(III) = 50 mg/L).

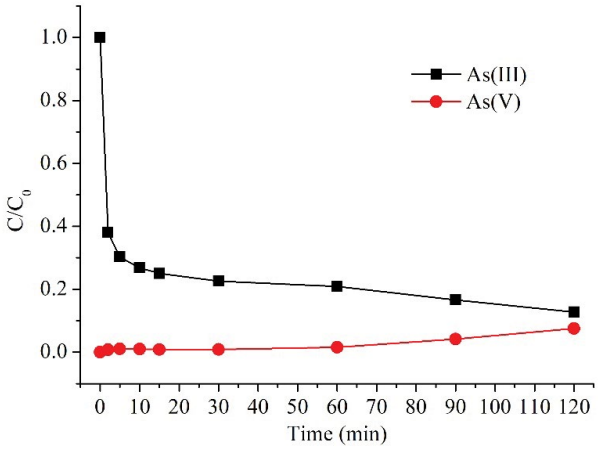

Fig. 7. Relationship between contact time and residual arsenic under CeO_2 at room temperature (experimental conditions: CeO_2 = 0.5 g, As(III) = 50 mg/L, and pH = 6.14).

$$\frac{t}{q_t} = \frac{1}{k_2 q_e^2} + \frac{t}{q_e} \tag{7}$$

where q_t (mg/g) is the CeO_2 amount at time t (min), q_e (mg/g) is the maximum adsorption capacity, and k_2 (g/mg min) is the rate constant. Applicability of the pseudo-second-order kinetic model is quantified by the squared correlation coefficient (R^2). Table 1 shows the kinetic parameters obtained from the data fitted in Fig. 8a. The high value of R^2 (0.9989) indicated that a pseudo-second-order kinetic model fitted the kinetics data accurately. Thus, it can be concluded that arsenic adsorption onto CeO_2 is driven by chemisorption involving valence forces through the sharing or exchange of electrons between CeO_2 and As(III) [26,42].

Two important adsorption isotherms, namely Langmuir and Freundlich, were fitted to the experimental data. Adsorption capacities of CeO_2 on As(III) were investigated by an equilibrium adsorption isotherm study as demonstrated in Fig. 8b. Adsorption data were fitted with Langmuir and Freundlich isotherms as Eqs. (8) and (9), respectively:

$$q_e = K_F C_e^{1/n} \tag{8}$$

$$q_e = \frac{q_{\max} K_L C_e}{1 + K_L C_e} \tag{9}$$

where q_e (mg/g) is the amount of the adsorbate adsorbed at the adsorbent, C_e (mg/L) is the equilibrium concentration of the adsorbate in solution, $q_{\max}$ (mg/g) is the maximum amount of the adsorbate adsorbed at the adsorbent at equilibrium time, K_L (L/mg) is a constant related to the heat of adsorption, K_F (mg/g) (L/mg)$^{1/n}$ is related to the adsorption capacity of the adsorbent of the adsorbent, and $1/n$ is a constant known as the heterogeneity factor that is related to the surface heterogeneity.

Compared to the Langmuir isotherm, the Freundlich isotherm plot resulted in a good fit with experimental data as evidenced in Fig. 8b. The Freundlich isotherm constants

Table 1
Adsorption kinetics and equilibrium adsorption isotherm fitting parameters for As(III) onto CeO_2

Adsorption kinetic (pseudo-second-order rate kinetic)			
Initial time (min)	15	30	60
q_e (mg/g)	0.086	0.081	0.079
k_2 (g/(mg min))	41.152	42.373	42.918
$h = k_2 q_e^2$ (mg/(g min)	0.304	0.278	0.267
R^2	0.9989	0.9994	0.9998
Equilibrium adsorption isotherm			
Freundlich	K_F (mg/g) (L/mg)$^{1/n}$	15.909	
	n	3.414	
	R^2	0.9856	
Langmuir	$q_{\max}$ (mg/g)	21.277	
	K_L (L/mg)	21.364	
	R^2	0.8424	

are shown in Table 1, and the linear correlation coefficients for As(III) of the plot were good. Fig. 8b shows the sorption isotherm in terms of As(III) in the solid phase as a function of equilibrium As(III) concentration in the leachate. The Freundlich isotherm fitted well for adsorption of As(III) on CeO_2. The "n" values of As(III) were observed to be more than the value 1, indicating that adsorption was favorable for As(III). However, the main assumption of the Freundlich model describes sorption on heterogeneous surfaces with sorption sites and heterogeneous energy distribution [38]. It also describes reversible adsorption which is not restricted to the formation of a monolayer [43].

Table 2 presents a comparison between our prepared CeO_2 and previously reported sorbents for As(III) sorption. Results demonstrated that CeO_2 outperformed many other sorbents. The high capacity indicated that our prepared CeO_2 was very effective for As(III) removal and achieved the aim of finding new materials that can combine oxidation and adsorption processes as an efficient method since

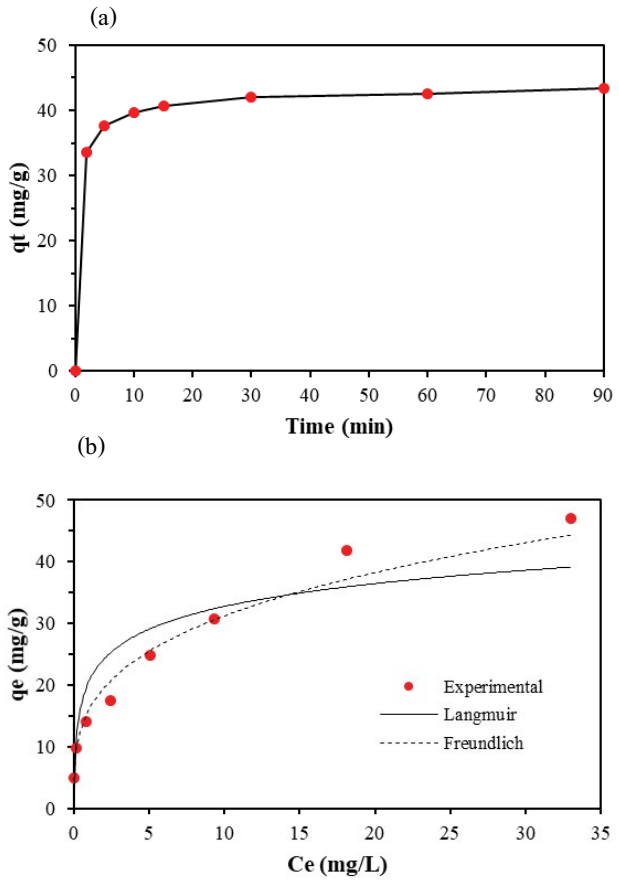

Fig. 8. Adsorption kinetic (a), and equilibrium adsorption isotherm of As(III) (b) on CeO_2 with high equilibrium concentration (experimental conditions: CeO_2 = 0.5 g, As(III) = 50 mg/L, and pH = 6.46).

As(III) is more toxic and more difficult to remove from water than As(V).

3.3. Adsorption mechanism and As(III) interaction on CeO_2

The XANES spectra are very sensitive to the oxidation state of the adsorbed atom; therefore, the As and Ce *K*-edge XANES spectra can indicate the oxidation state of elements that occur on the interface of materials between, before, and after arsenic removal at 120 min. Fig. 9a presents the normalized As *K*-edge XANES spectra of samples before and after the adsorption processes at different calcination temperatures (250°C and 550°C). The XANES features of the starting material were typical of As(III) and As(V) standard as 11,870.3 and 11,873.3 eV, respectively. The As *K*-edge of both CeO_2 samples (250°C and 550°C) showed that spectrum properties matched with the As(III) standard, while characteristics of the spectrum represented As(V) on the CeO_2 surface were similar to the As(V) standards. The As *K*-edge XANES data identified a combination of As(III) and traces of As(V) on the surface of CeO_2 since As(III) can be oxidized to As(V) on the surface of CeO_2 to a certain extent through the redox reaction of Ce^{4+}. Dahle et al. [49] noted that CeO_2 had a particularly high oxygen storage capacity; when coupled with its ease of transition between trivalent and tetravalent states and its high natural abundance, this makes CeO_2 an excellent choice as a catalyst 49].

The Ce L_3-edge was also examined by XANES after the adsorption processes. The results are shown in Fig. 9b, along with spectra for $Ce(NO_3)_3{\cdot}6H_2O$ (reference for Ce^{3+}) at 5,726.19 eV and CeO_2 powder (reference for Ce^{4+}) with double peaks at 5,730.59 and 5,737.40 eV, respectively. Before and after adsorption processes identified combinations of Ce^{4+} and slight Ce^{3+} due to the transmission of electrons between Ce^{4+} and As(III), resulting in the change of As(III) on the surface of CeO_2 as shown in Eq. (9).

$$2CeO_2 + 3H_3AsO_3 \rightarrow H_3AsO_4 + 2CeAsO_3 + H_2O \quad (9)$$

As(III) was oxidized to As(V) by receiving electrons from the CeO_2 redox reaction, and CeO_2 was reduced to Ce_2O_3 as a Ce^{4+} intermediate reaction product. This generated Ce_2O_3 which also oxidized As(III) to As(V). Results of Ce L_3-edge XANES spectra analysis inferred that CeO_2 played the role of an arsenic species adsorbent and acted as an oxidant.

The XANES analysis suggested possible adsorption mechanisms for As(III) removal by CeO_2 as shown in Fig. 10. Our results and existing reports concurred with As(III) adsorption on the hydroxyl group bond on the surface (Ce-OH) after the reaction. This was consistent with FTIR analysis revealing that functional groups such as -OH and

Table 2
Comparison of adsorption capacity of arsenite by various adsorbents

Adsorbent	Surface area (m^2/g)	Solution pH	Sorbate	Sorption capacity (mg/g)	Reference
MnBT-4	229	3	As(III)	27.4	[44]
Hematite NPS	–	7–8	As(III)	4.122	[45]
HyFe-MMT	277–355	9–7	As(III)	3.854	[46]
Ce-Loaded cationic resin	–	5–6	As(III), As(V)	2.25, 1.02	[47]
Ce-CNB	–	8	As(III)	57.5	[37]
NCMO	116.96	6–8	As(III)	34.89	[11]
CeO_2 NPS	–	7.0	As(III)	20.21	[48]
CeO_2 LCT	≈67.5	5.8–6.3	As(III)	21.27	This study

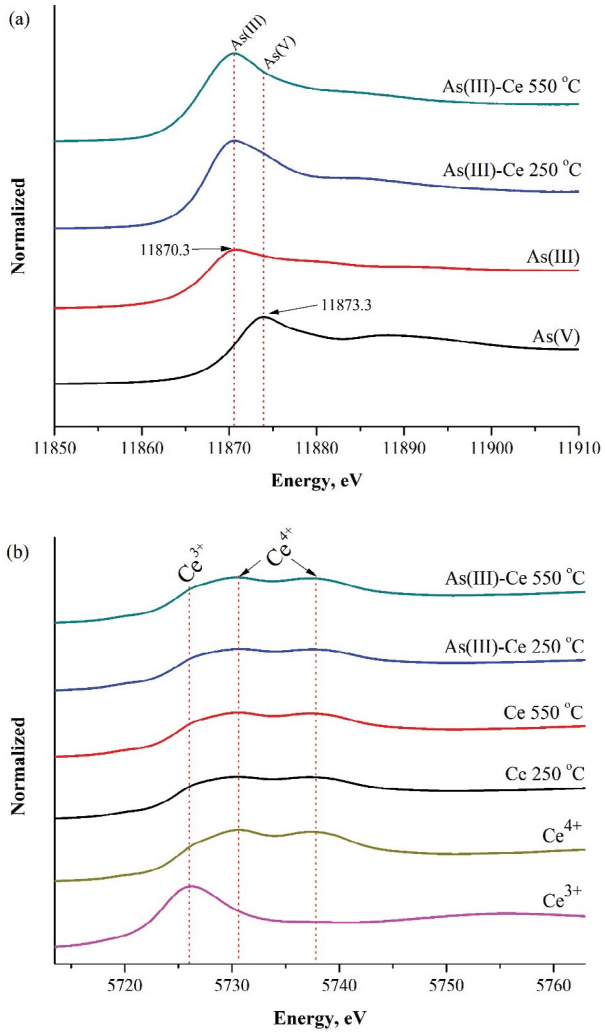

Fig. 9. Normalized XANES spectra for (a) As *K*-edge XANES spectra, and (b) Ce L_3-edge XANES spectra.

C-OH were involved in the adsorption of As(III) ions on CeO_2 [37,41,50] due to the formation of highly hydroxylated As(III) complexes via the reaction between Ce-OH and As-OH. The fast adsorption kinetics in this study indicated a chemisorption mechanism [26]. Thus, we suggest that As(III) adsorption occurs by forming inner-sphere complexes at the hydroxy group on the CeO_2 surface. Adsorption behavior that is unaffected by pH provides evidence for inner-sphere complexation, whereby the As(III) species exchanges with -OH groups that are directly coordinated to the CeO_2 surface. Possible monodentate and bidentate surface complexes allow CeO_2 to adsorb As(III) through a rapid and efficient process [26].

Based on an analysis using relationships between contact time and the XANES method, the As(III) on the surface of CeO_2 was partially oxidized to As(V), and then adsorbed onto CeO_2 at the experimental condition through two mechanisms [37] of surface complexation and redox reaction of CeO_2–Ce_2O_3. As(III) was oxidized to As(V) by receiving electrons from the CeO_2 redox reaction and CeO_2 was reduced to Ce_2O_3 as a Ce^{4+} intermediate reaction product. This generated Ce_2O_3 which also oxidized As(III)–As(V) as shown in Fig. 10. Thus, the main mechanism of As(III) adsorption was as follows: (i) complexation was conducted between hydroxyl groups on CeO_2 to form monodentate and bidentate complexes, and (ii) As(III) was oxidized to As(V) by redox reaction [37].

4. Conclusions

Our results indicated that CeO_2 was successfully synthesized following a simple precipitation process, with low-temperature calcination to adsorb As(III) in aqueous solution. Ceria being calcined at 250°C showed maximum adsorption capacities of As(III) reaching 21.27 mg/g. The adsorption behavior of As(III) was well-fitted to the Freundlich isotherm and a pseudo-second-order model. Analysis of XANES spectra demonstrated that oxidation states of Ce and As occurred on the interface of materials between, before,

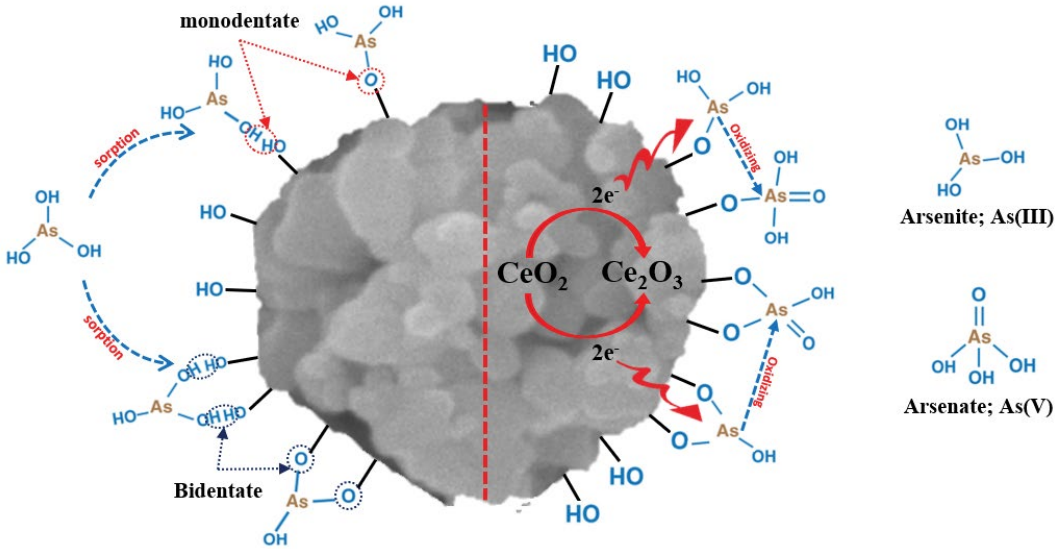

Fig. 10. Schematic diagram for the proposed mechanism of As(III) adsorption and As(III) oxidation to As(V) on the surface of CeO_2.

and after arsenic removal. The As(III) adsorption mechanisms as complexation were conducted between hydroxyl groups and redox transformation between As(III) and CeO_2. Our results suggested that economical synthesis of CeO_2 offers potential as an efficient method for removal of As(III) from polluted water by adsorption.

Acknowledgments

This work was financially supported by the Research and Technology transfer affairs of Khon Kaen University, The Thailand Research Fund (MRG6180196), and Office of the Higher Education Commission. The authors also would like to acknowledge the Synchrotron Light Research Institute (Public Organization) and Research Program on Development of Appropriate Technologies for Coloring Agent Removal from Textile Dyeing, Pulp & Paper, Sugar Industries for Sustainable Management, Center of Excellence on Hazardous Substance Management (HSM), Chulalongkorn University, Thailand.

References

[1] D. Liu, S. Deng, A. Maimaiti, B. Wang, J. Huang, Y. Wang, G. Yu, As(III) and As(V) adsorption on nanocomposite of hydrated zirconium oxide coated carbon nanotubes, J. Colloid Interface Sci., 511 (2018) 277–284.
[2] E. Şık, E. Demirbas, A.Y. Goren, M.S. Oncel, M. Kobya, Arsenite and arsenate removals from groundwater by electrocoagulation using iron ball anodes: influence of operating parameters, J. Water Process Eng., 18 (2017) 83–91.
[3] L. Al-Eryani, S. Waigel, V. Jala, S.F. Jenkins, J.C. States, Cell cycle pathway dysregulation in human keratinocytes during chronic exposure to low arsenite, Toxicol. Appl. Pharmacol., 331 (2017) 130–134.
[4] Z. Cheng, F. Fu, D.D. Dionysiou, B. Tang, Adsorption, oxidation, and reduction behavior of arsenic in the removal of aqueous As(III) by mesoporous Fe/Al bimetallic particles, Water Res., 96 (2016) 22–31.
[5] B.R.C. Vieira, A.M.A. Pintor, R.A.R. Boaventura, C.M.S. Botelho, S.C.R. Santos, Arsenic removal from water using iron-coated seaweeds, J. Environ. Manage., 192 (2017) 224–233.
[6] A. Sarkar, B. Paul, The global menace of arsenic and its conventional remediation – a critical review, Chemosphere, 158 (2016) 37–49.
[7] L. Lin, W. Qiu, D. Wang, Q. Huang, Z. Song, H.W. Chau, Arsenic removal in aqueous solution by a novel Fe-Mn modified biochar composite: characterization and mechanism, Ecotoxicol. Environ. Saf., 144 (2017) 514–521.
[8] A. Adra, G. Morin, G. Ona-Nguema, J. Brest, Arsenate and arsenite adsorption onto Al-containing ferrihydrites. Implications for arsenic immobilization after neutralization of acid mine drainage, Appl. Geochem., 64 (2015) 2–9.
[9] S. Martinez-Vargas, A.I. Martínez, E.E. Hernandez-Beteta, O.F. Mijangos-Ricardez, V. Vazquez-Hipolito, C. Patino-Carachure, J. Lopez-Luna, As(III) and As(V) adsorption on manganese ferrite nanoparticles, J. Mol. Struct., 1154 (2018) 524–534.
[10] Y. Xiong, Q. Tong, W. Shan, Z. Xing, Y. Wang, S. Wen, Z. Lou, Arsenic transformation and adsorption by iron hydroxide/manganese dioxide doped straw activated carbon, Appl. Surf. Sci., 416 (2017) 618–627.
[11] K. Gupta, S. Bhattacharya, D. Nandi, A. Maity, A. Mukhopadhyay, D.J. Chattopadhyay, N.R. Ray, P. Sen, U.C. Ghosh, Arsenic(III) sorption on nanostructured cerium incorporated manganese oxide (NCMO): a physical insight into the mechanistic pathway, J. Colloid Interface Sci., 377 (2012) 269–276.
[12] Y.M. Zheng, L. Yu, D. Wu, J.P. Chen, Removal of arsenite from aqueous solution by a zirconia nanoparticle, Chem. Eng. J., 188 (2012) 15–22.
[13] K. Shehzad, C. Xie, J. He, X. Cai, W. Xu, J. Liu, Facile synthesis of novel calcined magnetic orange peel composites for efficient removal of arsenite through simultaneous oxidation and adsorption, J. Colloid Interface Sci., 511 (2018) 155–164.
[14] S. Khuntia, S.K. Majumder, P. Ghosh, Oxidation of As(III) to As(V) using ozone microbubbles, Chemosphere, 97 (2014) 120–124.
[15] J. Qin, H. Li, C. Lin, Fenton process-affected transformation of roxarsone in paddy rice soils: effects on plant growth and arsenic accumulation in rice grain, Ecotoxicol. Environ. Saf., 130 (2016) 4–10.
[16] J. Qin, Y. Li, M. Feng, H. Li, C. Lin, Fenton reagent reduces the level of arsenic in paddy rice grain, Geoderma, 307 (2017) 73–80.
[17] S. Crognale, B. Casentini, S. Amalfitano, S. Fazi, M. Petruccioli, S. Rossetti, Biological As(III) oxidation in biofilters by using native groundwater microorganisms, Sci. Total Environ., 651 (2019) 93–102.
[18] Y. Sun, G. Liu, Y. Cai, Thiolated arsenicals in arsenic metabolism: occurrence, formation, and biological implications, J. Environ. Sci., 49 (2016) 59–73.
[19] A. Samad, M. Furukawa, H. Katsumata, T. Suzuki, S. Kaneco, Photocatalytic oxidation and simultaneous removal of arsenite with CuO/ZnO photocatalyst, J. Photochem. Photobiol., A, 325 (2016) 97–103.
[20] K.B. Fontana, G.G. Lenzi, E.C.R. Seára, E.S. Chaves, Comparision of photocatalysis and photolysis processes for arsenic oxidation in water, Ecotoxicol. Environ. Saf., 151 (2018) 127–131.
[21] X. Zhao, B. Zhang, H. Liu, J. Qu, Removal of arsenite by simultaneous electro-oxidation and electro-coagulation process, J. Hazard. Mater., 184 (2010) 472–476.
[22] X. Han, J. Song, Y.L. Li, S.Y. Jia, W.H. Wang, F.G. Huang, S.H. Wu, As(III) removal and speciation of Fe(Oxyhydr)oxides during simultaneous oxidation of As(III) and Fe(II), Chemosphere, 147 (2016) 337–344.
[23] X. Xie, Y. Liu, K. Pi, C. Liu, J. Li, M. Duan, Y. Wang, *In situ* Fe-sulfide coating for arsenic removal under reducing conditions, J. Hydrol., 534 (2016) 42–49.
[24] L. Fan, S. Zhang, X. Zhang, H. Zhou, Z. Lu, S. Wang, Removal of arsenic from simulation wastewater using nano-iron/oyster shell composites, J. Environ. Manage., 156 (2015) 109–114.
[25] O. Eljamal, K. Sasaki, S. Tsuruyama, T. Hirajima, Kinetic model of arsenic sorption onto zero-valent iron (ZVI), Water Qual. Exposure Health, 2 (2011) 125–132.
[26] R. Li, Q. Li, S. Gao, J. Ku, Exceptional arsenic adsorption performance of hydrous cerium oxide nanoparticles: Part A. Adsorption capacity and mechanism, Chem. Eng. J., 186 (2012) 127–135.
[27] T. Arii, T. Taguchi, A. Kishi, M. Ogawa, Y. Sawada, Thermal decomposition of cerium(III) acetate studied with sample-controlled thermogravimetric-mass spectrometry (SCTG-MS), J. Eur. Ceram. Soc., 22 (2002) 2283–2289.
[28] Y. Yu, C. Zhang, L. Yang, J.P. Chen, Cerium oxide modified activated carbon as an efficient and effective adsorbent for the rapid uptake of arsenate and arsenite: material development and study of performance and mechanisms, Chem. Eng. J., 315 (2016) 630–638.
[29] J. Phanthasri, P. Khamdahasag, P. Jutaporn, K. Sorachoti, K. Wantala, V. Tanboonchuy, Enhancement of arsenite removal using manganese oxide coupled with iron(III) trimesic, Appl. Surf. Sci., 427 (2018) 545–552.
[30] P. Janos, P. Kuran, M. Kormunda, V. Stengl, T.M. Grygar, M. Dosek, M. Stastny, J. Ederer, V. Pilarova, L. Vrtoch, Cerium dioxide as a new reactive sorbent for fast degradation of parathion methyl and some other organophosphates, J. Rare Earths, 32 (2014) 360–370.
[31] E.K. Goharshadi, S. Samiee, P. Nancarrow, Fabrication of cerium oxide nanoparticles: Characterization and optical properties, J. Colloid Interface Sci., 356 (2011) 473–480.
[32] L.T. Murciano, A. Gilbank, B. Puertolas, T. Garcia, B. Solsona, D. Chadwick, Shape-dependency activity of nanostructured CeO_2 in the total oxidation of polycyclic aromatic hydrocarbons, Appl. Catal., B, 133 (2013) 116–122.

[33] H.L. Chen, H.Y. Chang, Synthesis of nanocrystalline cerium oxide particles by the precipitation method, Ceram. Int., 31 (2005) 795–802.
[34] S.J.M. Rosid, W.A.W.A. Bakar, R. Ali, Characterization and modelling optimization on methanation activity using Box–Behnken design through cerium doped catalysts, J. Cleaner Prod., 170 (2018) 278–287.
[35] W.E. Mahmoud, A. Faidah, Microwave assisted hydrothermal synthesis of engineered cerium oxide nanopowders, J. Eur. Ceram. Soc., 32 (2012) 3537–3541.
[36] S. Cheng, L. Zhang, A. Ma, H. Xia, J. Peng, C. Li, J. Shu, Comparison of activated carbon and iron/cerium modified activated carbon to remove methylene blue from wastewater, J. Environ. Sci., 5 (2017) 1–11.
[37] L. Zhang, T. Zhu, X. Liu, W. Zhang, Simultaneous oxidation and adsorption of As(III) from water by cerium modified chitosan ultrafine nanobiosorbent, J. Hazard. Mater., 308 (2016) 1–10.
[38] J. Chen, J. Wang, G. Zhang, Q. Wu, D. Wang, Facile fabrication of nanostructured cerium-manganese binary oxide for enhanced arsenite removal from water, Chem. Eng. J., 334 (2018) 1518–1526.
[39] J.J. Ketzial, A.S. Nesaraj, Synthesis of CeO_2 nanoparticles by chemical precipitation and the effect of a surfactant on the distribution of particle sizes, J. Ceram. Process. Res., 12 (2011) 74–79.
[40] D. Vovchok, C.J. Guild, S. Dissanayake, J. Llorca, E. Stavitski, Z. Liu, R.M. Palomino, Y. Li, A.I. Frenkel, J.A. Rodriquez, S.L. Suib, S.D. Senanayake, *In situ* characterization of mesoporous Co/CeO_2 catalysts for the high-temperature water-gas shift, J. Phys. Chem. C., 122 (2018) 8998–9008.
[41] D.R. Mullins, The surface chemistry of cerium oxide, Surf. Sci. Rep., 70 (2015) 42–85.
[42] C. Feng, C. Aldrich, J.J. Eksteen, D.W.M. Arrigan, Removal of arsenic from gold cyanidation process waters by use of cerium-based magnetic adsorbents, Miner. Eng., 122 (2018) 84–90.
[43] M. Attari, S.S. Bukhari, H. Kazemian, S. Rohani, A low-cost adsorbent from coal fly ash for mercury removal from industrial wastewater, J. Environ. Chem. Eng., 5 (2017) 391–399.
[44] Y.H. Huang, Y.J. Shih, F.J. Cheng, Novel $KMnO_4$-modified iron oxide for effective arsenite removal, J. Hazard. Mater., 198 (2011) 1–6.
[45] D. Dickson, G. Liu, Y. Cai, Adsorption kinetics and isotherms of arsenite and arsenate on hematite nanoparticles and aggregates, J. Environ. Manage., 186 (2017) 261–267.
[46] D.A. Almasri, T. Rhadfi, M.A. Atieh, G. McKay, S. Ahzi, High performance hydroxyiron modified montmorillonite nanoclay adsorbent for arsenite removal, Chem. Eng. J., 335 (2018) 1–12.
[47] H. Zongliang, T. Senlin, N. Ping, Adsorption of arsenate and arsenite from aqueous solutions by cerium-loaded cation exchange resin, J. Rare Earths, 30 (2012) 563–572.
[48] C. Zeng,C. Nguyen, S. Boitano, J.A. Field, F. Shadman, R. Sierra-Alvarez, Cerium dioxide (CeO_2) nanoparticles decrease arsenite (As(III)) cytotoxicity to 16HBE14o-human bronchial epithelial cells, Environ. Res., 164 (2018) 452–458.
[49] J.T. Dahle, Y. Arai, Environmental geochemistry of cerium: applications and toxicology of cerium oxide nanoparticles, Int. J. Environ. Res. Public Health, 12 (2015) 1253–1278.
[50] B.M. Harish, M.P. Rajeeva, V.S. Chaturmukha, S. Suresha, H.S. Jayanna, S. Yallappa, A.R. Lammani, Influence of zinc on the structural and electrical properties of cerium oxide nanoparticles, Mater. Today Proc., 5 (2018) 3070–3077.